Draft version September 28, 2025
Typeset using LaTeX **twocolumn** style in AASTeX631

Investigating the 3D Atmospheric Structure of a Free-Floating Exoplanet Analog through Spectrophotometric Variability

Logan Bennett,[1] Max Millar-Blanchaer,[2] and Connor Vancil[2]

[1] *Department of Physics, The College of New Jersey*
[2] *Department of Physics, University of California, Santa Barbara*

ABSTRACT

Young, low-mass brown dwarfs serve as analogs to giant exoplanets otherwise too heavily obscured by the light of their host stars. With comparable radii, effective temperatures, and surface gravities, these free-floating planetary mass objects provide valuable opportunities for atmospheric observation and characterization. Therefore, studies of planet-like brown dwarfs are applicable to the giant exoplanets that we cannot yet observe with precision. Tracking variability across multiple rotational periods with direct spectrophotometric observations allows us to build a three-dimensional model of an object's atmosphere. Our target is T2.5, 12.7 $M_{\rm Jup}$, free-floating object SIMP J013656.5+093347.3 (SIMP0136), and we analyze two nights of *Keck I/MOSFIRE* observations in the J-band taken in September and November, 2024. SIMP0136 was chosen as a target for its similarity to many directly imaged exoplanets, as well as its previously observed variability of up to and greater than 4% in the J-band. Our analysis includes over 4 full rotational periods between both nights, and we confirm similar variability across the J-band. We investigate differences in variability between the 1.24 μm doublet and the continuum, probing different atmospheric depths and weighing evidence whether this points to differential rotation, or homogeneous movement between cloud layers. We find differences in the light curves between both nights and previous literature observations, which may point to an evolving atmosphere. The results of this investigation provide insight on the atmospheric structure of a transitioning brown dwarf for further confirmation of long-term cloud evolution and more detailed mapping of the atmosphere of a planetary mass object.

Keywords: Spectrophotometric variability, brown dwarfs, exoplanet atmospheres

1. INTRODUCTION

A brown dwarf is a substellar object typically found with a mass between $\sim 0.01 M_\odot$ but never exceeding the hydrogen burning limit of $\sim 0.075 M_\odot$ (Luhman 2012). Brown dwarfs cannot sustain fusion and, as a result, will continue to cool and condense throughout their lifetimes. Clouds begin to form in the atmospheres of these objects below an effective temperature of $\leq 2,800$K, giving them a planet-like spectrum early in their life (Helling & Casewell 2014). The features of young brown dwarfs make them excellent analogs to giant planets we have found of similar size, mass, and surface gravities. This opens up great opportunities for comparison to the atmospheric dynamics of directly imaged exoplanets (Faherty et al. 2013).

Studies of planets beyond our solar system are of great interest, but the depth of information we can gather is limited by the method by which they are observed. Although techniques such as radial velocity and transit are responsible for the majority of exoplanet discoveries and therefore data, the smaller group of planets observed with direct images provide unambiguous spectra when it can be resolved. However, direct observations of exoplanets are often heavily obscured by the light of their host stars, making spectrophotometric measurements, useful for atmosphere characterization, difficult to discern. It is possible for a brown dwarf to form independently and isolated, classifying them as free-floating planetary-mass objects. Unobscured by the light of a host star, these objects provide us with the opportunity to examine atmospheric processes in much finer detail.

1.1. *Spectrophotometric Variability*

Collecting photometric measurements over a range of wavelengths and over the period of that object's rotation, either through thermal radiation from the interior of an object or through the process of starlight passing

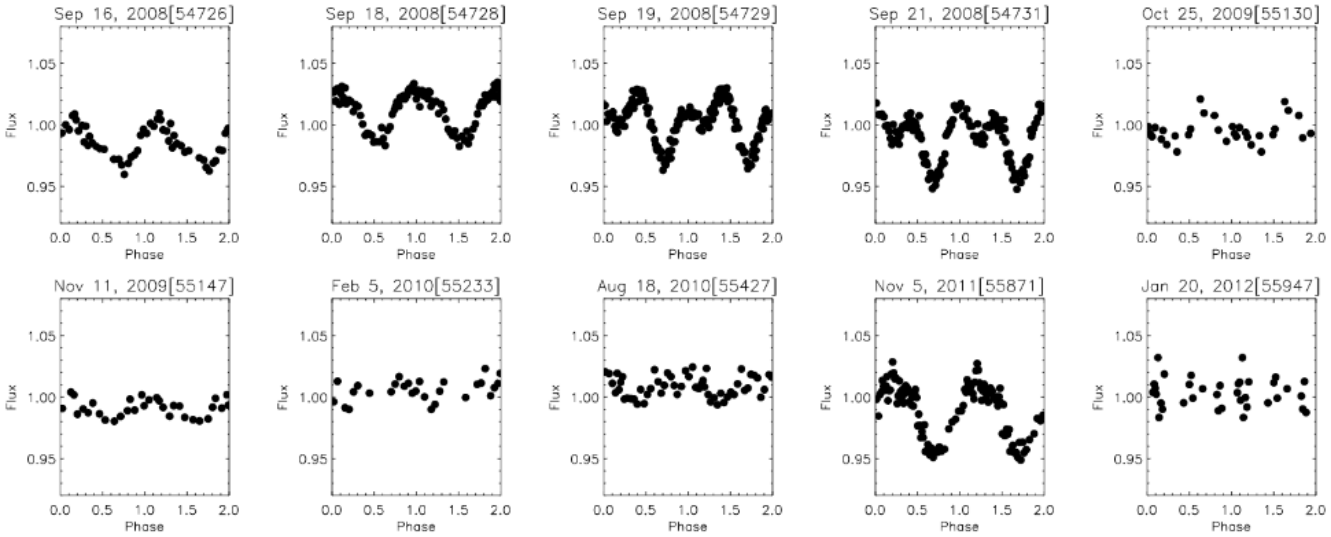

Figure 1: Metchev et al. (2013) tracks the long-term spectral variability of SIMP0136 in the J-band. The light curves are folded to the rotational period of $\sim$ 2.4hr. The fact that these variability curves change point towards atmospheric evolution.

through an object's atmosphere, allows us to probe variability at various heights. In the case of a free-floating object, these photons are emitted thermally, with the continuum of a spectrum representing no absorption and absorption features representing the presence of clouds. These features are sensitive to their atmospheric height, or pressure, and if we track the change in flux of these absorption features through multiple periods of rotation, then we can determine how the opacity of that layer changes. We then use atmospheric modeling to determine where these layers of cloud decks should be. Little to no photometric variability in a known cloud deck can imply the existence of homogeneous cloud coverage, while larger amounts of variability can point to patchy clouds, hot-spots, or aurorae.

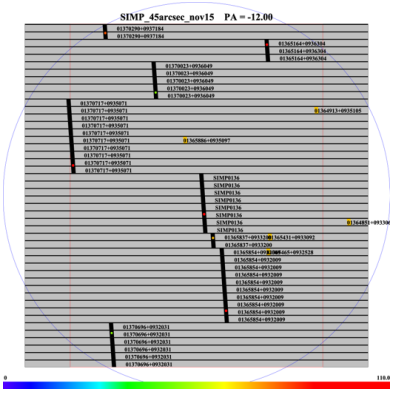

Figure 2: The pre-rotated slit mask used in November observations, though identical to the mask used in September

1.2. *Observations of SIMP J013656.5+093347.3*

SIMP J013656.5+093347.3 (SIMP0136) is a planetary-mass (12.7 M_{Jup}) brown dwarf with a similar age and mass to many directly imaged exoplanets (Gagné et al. 2017). SIMP0136 has previously shown long-term variability of up to 4% in the J-band (Fig.1) which could be indicative of long-term atmospheric evolution. These factors contributed to its selection as the target for observations in 2021 and 2023; although, these nights were plagued by bad weather, instrumental issues, and unlucky periods of no variability. SIMP0136 was again observed in September and November of 2024 for a total of more than 13 hours. With a rotational period of $\sim$2.4 hours, each night is comprised of nearly 3 full rotations. Observations were made using the *MOSFIRE* multi-slit spectrograph on the 10m Keck 1 telescope at the W.M. Keck Observatory, and the slit mask used can be seen in Fig.2.During the November observations, an instrumental issue required the use of a 180 degree, rotated slit mask which will be discussed further in 2.1 As one of the only medium-resolution spectroscopic studies on a brown dwarf, we hope to resolve more pressure layers using individual lines such as the K-I doublet, which might have previously been blended into the continuum of lower resolution spectrographic data.

2. METHODS

2.1. *Data Reduction*

We utilized the Python package *PypeIt*, a semi-automated data reduction pipeline for spectroscopic ob-

servations, to perform much of the processing of the science images for both nights of data (Prochaska et al. 2020). *PypeIt* creates a master flat, performs sky subtraction, and automatically produces a wavelength calibration using the designated arc frames. Arc frames were taken in both nights using 1.0" slits, while science frames were taken with wider 4.5" slits. We did not notice any negative effects of using the rotated slit mask. The only difference was a reversed order of objects in the processed FITS headers. We followed the instructions given by *PypeIt* to use the smaller slit frames to calculate the wavelength calibration then used in the reduction of the wider slit data. Performing the wavelength calibration with the wider slit arc frames produced an RMS value of ≈0.8 Å, but the smaller slit data produced RMS values for both nights below 0.1 Åwhich is within the range recommended by *PypeIt*. We calculate the SNR for both nights of data for every object by finding the maximum value of counts divided by their respective error in each frame, then taking the median across frames. These values can be found in Table 1. *MOSFIRE* observations are able to use a dithering pattern when taking exposures, and an ABAB pattern was used across both nights. Due to this movement pattern, the spectra are physically shifted, so we decided that it would be necessary to co-add each A-B pair to remove this shift and improve sky subtraction. This co-addition can be performed automatically by *PypeIt* with the *coadd2d* command. where the 1-D spectra are then extracted from the 2-D images produced. Co-addition also places the pairs onto a common, linear wavelength grid created from the individual frames; and, while each new frame is not on the exact same wavelength grid as the frame next to it, these differences will be addressed in the following section.

2.2. *Light Curve Production*

To accurately produce light curves across multiple wavelength regions, every object must be aligned on the same wavelength grid. For everything beyond this point, a 1.2 - 1.3 micron wavelength mask was applied due to heavy telluric contamination beyond this range. Using the wavelength grid of the SIMP0136 slit in the first frame, every object across all frames was interpolated to that grid. Within each frame, a cross-correlation function was then used to shift all of the reference star spectra to align with the absorption features of SIMP0136 in that frame. Similar cross-correlation was then performed by matching the absorption features of every SIMP0136 spectra with that of the first frame of the night, and applying this same shift to every reference star within the frame. This leaves every object across the night on the same wavelength grid with a separation of ~ 1.299 Å per pixel.

To produce corrected and normalized light curves, we use the following process, similar to that of Manjavacas et al. 2021: We find the sum of counts within the specified wavelength range for each object in every frame. We take the median across all frames of these sums for each object, and each objects raw sum is then divided by its respective median, creating median divided light curves for every object. The median divided sum of SIMP0136 in each frame is then divided by the median of the median divided reference stars used, creating the corrected light curve. The corrected light curve for reference stars is found in the same manner; however, SIMP0136 is not used in its division, nor is itself. To normalize each light curve, we divide by its median of corrected values across all frames.

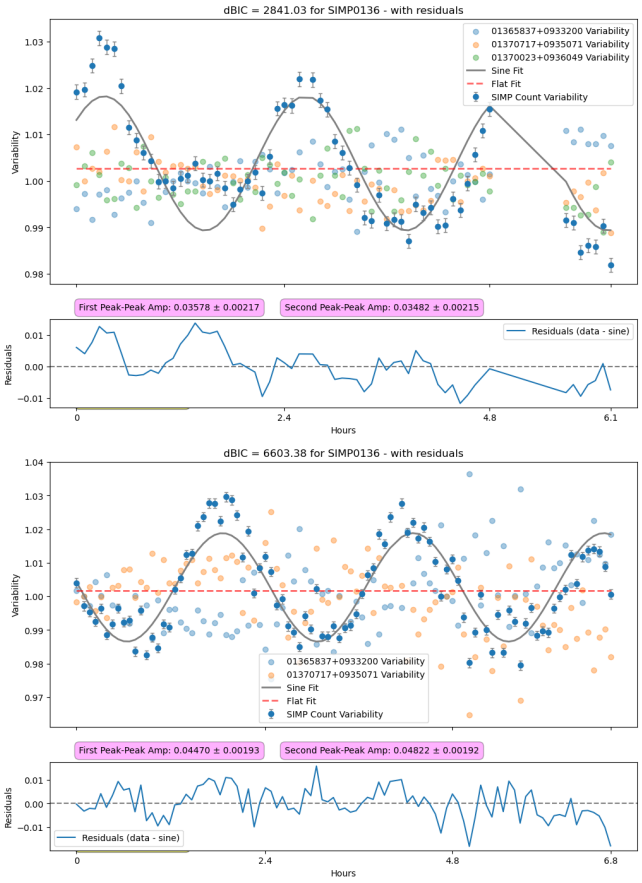

Figure 3: September (top) and November (bottom): Corrected and normalized light curve of SIMP0136 showing which reference stars are used in the division as well as the results of the BIC test.

Object	J-Band Mag	Uncorrected σ	σ in SIMP Units	Corrected σ (counts)	σ in SIMP Units	SNR
SIMP0136	13.45	1.5e-2	1	1.1e-2	1	120.5
01370696+0932031	No data	1.1e-2	0.737	9e-3	0.828	67.1
01365854+0932009	No data	9e-3	0.558	7e-3	0.611	66.1
01365837+0933200	No data	1.1e-2	0.733	7e-3	0.627	72.3
01370717+0935071	13.42	9e-3	0.574	3e-3	0.290	52.8
01370023+0936049	No data	1.1e-2	0.717	6e-3	0.503	75.4
01365164+0936304	14.29	9e-3	0.581	5e-3	0.457	65.2
01370290+0937184	12.72	50.87	3287.6	50.46	4521.4	43.6
SIMP0136	13.45	0.104	1	1.5e-2	1	116.0
01370696+0932031	No data	0.105	1.008	2.2e-2	1.491	72.1
01365854+0932009	No data	0.103	0.987	9e-3	0.618	70.5
01365837+0933200	No data	0.101	0.967	1.4e-2	0.932	72.2
01370717+0935071	13.42	0.106	1.02	1e-2	0.692	57.4
01370023+0936049	No data	0.140	1.343	4.4e-2	2.982	77.9
01365164+0936304	14.29	0.109	1.047	2e-2	1.335	70.9
01370290+0937184	12.72	0.122	1.166	2.5e-2	1.653	46.0

Table 1: Objects with their uncorrected and corrected standard deviation. This is also expressed in SIMP units ($\sigma_{star}/\sigma_{SIMP}$). The SNR is also listed on the right. The top half of the table is for September, while the bottom is for November.

2.3. *Reference Star Selection*

Due to the high J-band magnitude, or simply lack of data, of the reference stars, they cannot be excluded based on previously known intrinsic variability. We calculate each objects standard deviation before and after performing light curve correction; although, while those with high σ can be discarded ($\sigma_{star} > 1.5\sigma_{SIMP}$), many reference stars are $\leq \sigma_{SIMP}$. We further test reference star variability through the Bayesian Information Criterion (BIC test). This model attempts to fit both a sine and a flat curve to the corrected light curve, assigning a lower score for a better fit. Subtracting the sine score from the flat score then gives the ΔBIC value, with a positive ΔBIC implying a variable source. Due to our ΔBIC values being >> those in similar studies, we have decided that only objects with ΔBIC> 50 can be confidently labeled as variable. Taking into account the BIC test in combination with considering σ, we selected reference stars 01365837+0933200, 01370717+0935071, and 01370023+0936049 for use in the analysis of the September data, without further including 01370023+0936049 in the analysis of the November observations. The corrected light curves with the results of the BIC test can be seen in figure 3.

3. RESULTS

Since each night contains two full periods, we have 4 total rotations to probe variability. We can use peak-to-peak values, or the difference between maximum and minimum values between peaks in the light curves. For the September data (Fig.3), we use the maximum of the first peak region and the minimum of the first trough region, then the same for the second peak and trough (we would like to note the unusual shape of the light curve within the first trough). This leads us to a first period variability of 0.03578 ± 0.00217 counts (3.578±0.217%), and a second period variability of 0.03482 ± 0.00215 counts (3.482±0.215%) for observations in September. To remain consistent in our calculations, we use the first peak and second trough, and second peak and third trough regions for finding the variability in November. For the first period, we obtain 0.04470 ± 0.00204 counts (4.470±0.204%), and for the second period we obtain, 0.04822 ± 0.00192 counts (4.822±0.192%). We probe the potassium doublet with absorption features found by their local minima, as seen in figures 8 and 9. We sum regions 30 Å on either side of these minima to account for the full absorption region. We also include the continuum between the lines, as well as 30 Å on the red and blue ends of the doublet to check if the variability is contained at the pressure level of the absorption features.

The peak-peak variability is calculated for the potassium doublet and the regions surrounding them in the same way as it is calculated for the J-band variability respective to each night. We also compare each night, taking the average of the two periods and taking the difference between September and November variability to check for evolution of the light curve. We compare the entire 1.2-1.3 μm range, the first potas-

sium line, and the second potassium line. For the full range we obtain an increase of 0.00992 ± 0.00293 counts (0.992±0.293%), while the differences between each potassium line amounts to negligible values.

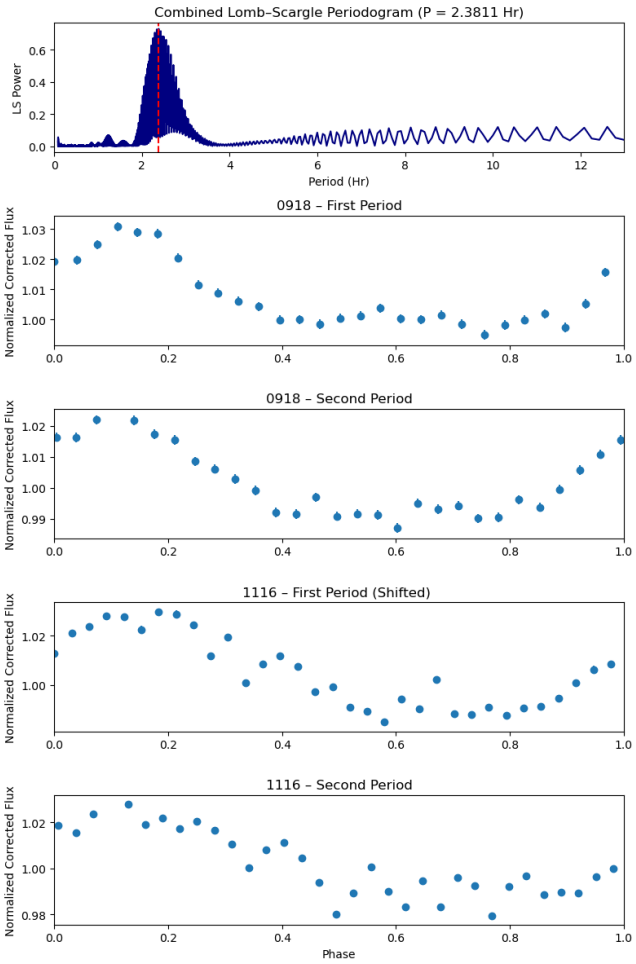

Figure 4: Lomb-Scargle periodogram created with the combined data of both nights of observation. Shows phase folded first and second periods of September as well as November. The November periods begin 20 frames into the night in order to match the shape of the September data.

We create a Lomb-Scargle periodogram (4) using the combined light curves between both nights of data to find the best fit period and phase-fold the periods of each night. We set the upper and lower bounds of the model as the combined observing time between both nights and the average time between exposures. The fit returns a period of 2.381 hours, aligning closely with previously observed periods close to 2.4 hours (Artigau et al. 2009). The two periods in each night are phase-folded in accordance with this period, and we plot them vertically to assess any visual evolution. The November light curves begin 20 frames into the night in order to start the phases near a maximum, as with the September observations. There appear to be slight period-period differences, but this would require further analysis.

4. INTERPRETING VARIABILITY REGIONS

We find peak-to-peak variability in the J-band, both lines of the potassium doublet, the continuum between them, and their blue and red ends for both nights of observations. While the variability in each of these regions per night are not exactly the same, they are similar to each other both in their magnitude and in the shape of their light curves.

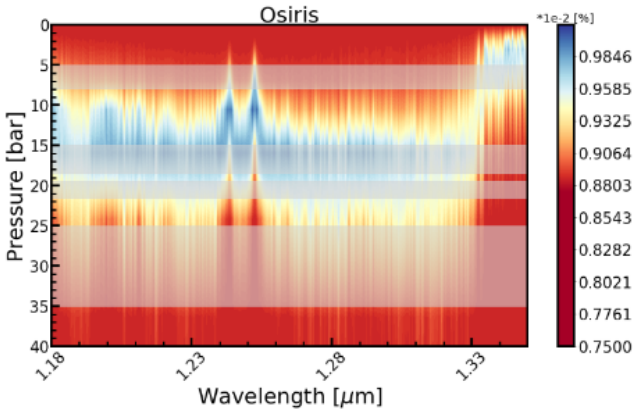

Figure 5: Modeled J-band observations in the atmosphere of SIMP0136 for the Osiris spectrograph. Shows the varying pressure levels which different wavelengths display the most absorption (blue). The potassium doublet can be seen noticeably spiking to ∼5 bar.

Figure 5 displays J-band observations in a simulated SIMP0136 atmosphere when observed with the Osiris spectrograph (not MOSFIRE, as used in this paper, but they slightly differ in spectral resolution). We see that the potassium doublet displays greater absorption at much lower pressures than the J-band continuum. This can potentially lead to the formation of separate cloud decks, although with both regions showing similar variability, we must assess their correlation. In figures 8 and 9 we find the Kendall rank correlation coefficient between the following regions: the first and second potassium line, each line and the continuum between them as well as the red and blue ends, both lines combined and the 1.2-1.3μm range. The correlation function compares the light curves of each pair and assesses the similarity of each point, with $\tau > 0$ and closer to 1 implying a strong correlation and a lower p-value labeling this correlation as statistically significant. We find strong, statistically

significant correlations between every region pair implying homogeneous variability and cloud layers between the potassium doublet and the continuum in both nights of observations.

It is important to note that variability may arise from other atmospheric events other than the presence of clouds. Apai et al. (2017) investigates variability patterns caused by planetary-scale bands and hot spots. The odd shape within the first trough in the September light curve is visually similar to what they found as hot spots, though more analysis is necessary.

5. CONCLUSIONS

We analyzed two nights of medium-resolution *Keck/MOSFIRE* *J*-band spectroscopy of SIMP0136, covering more than four full rotations with more than two periods each night, confirming a period of 2.381 hours, consistent with previous findings (Artigau et al. 2009). We confirm variability at the 3–5% level consistent with previous photometric and spectroscopic observations (Metchev et al. 2013), and we detect this variability across both the continuum and the potassium doublet absorption features. The variability amplitudes differ slightly between September and November, providing evidence for long-term atmospheric evolution. The similar shapes of the light curves and the strong correlations between absorption and continuum regions indicate largely homogeneous variability across pressure levels, rather than evidence for differential rotation. The differences in light-curve shape between the first and second September periods suggest that atmospheric evolution may occur on timescales as short as one rotation.

Looking towards the future of this project, we will send our data to atmospheric modelers to construct a more detailed understanding of the possible composition at different pressure levels. We will also perform more in-depth studies on the full spectra from both nights of data, analyzing change per-wavelength rather than summing over wavelength ranges.

Our results add to the growing evidence that cloud evolution plays a central role in the variability of L/T transition brown dwarfs, as well as continuing our understanding of atmospheric studies on planetary mass objects. Continued monitoring with medium-resolution spectroscopy can help further disentangle the contributions of cloud structure, atmospheric dynamics, and other processes such as hot spots or planetary-scale waves, ultimately improving our three-dimensional understanding of brown dwarf and exoplanet atmospheres.

6. ACKNOWLEDGMENTS

I would like to thank Professor Millar-Blanchaer for his leadership in this project and guidance during the most challenging portions of working with this data. I also thank Connor Vancil for his day-to-day guidance through this work and his constant assistance with any question that arose. The REU program itself would not be possible without Professor Guruswamy, the site director, to whom I extend my gratitude. None of my progress would have been possible without the combined effort of these three. This work is supported by NSF REU grant PHY-2349677.

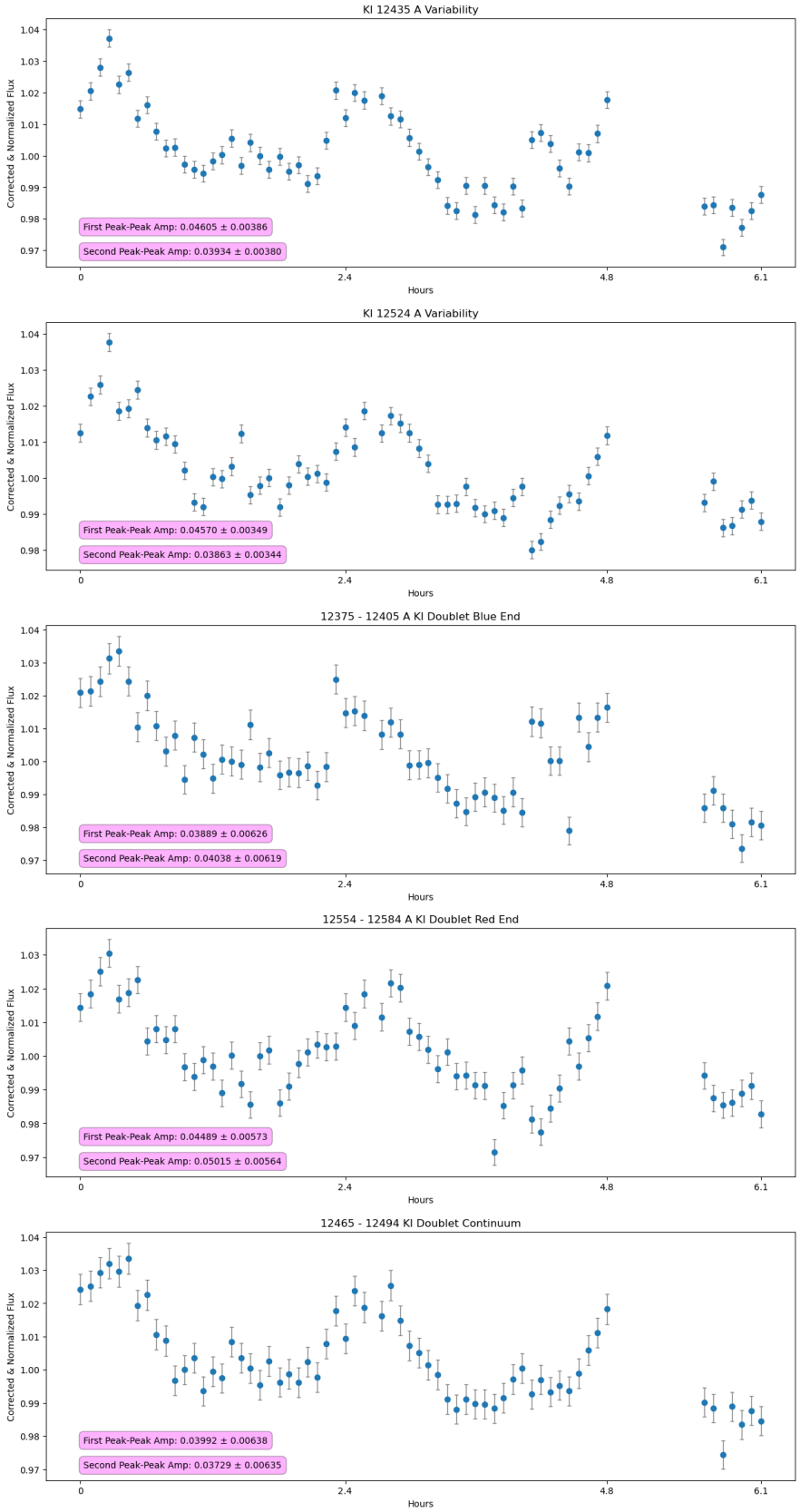

Figure 6: For September: Variability of the potassium doublet absorption lines (first then second), variability of 30 Å on the blue end of the doublet, variability of 30 Å on the red end of the doublet, and variability of the continuum between the first and second absorption lines.

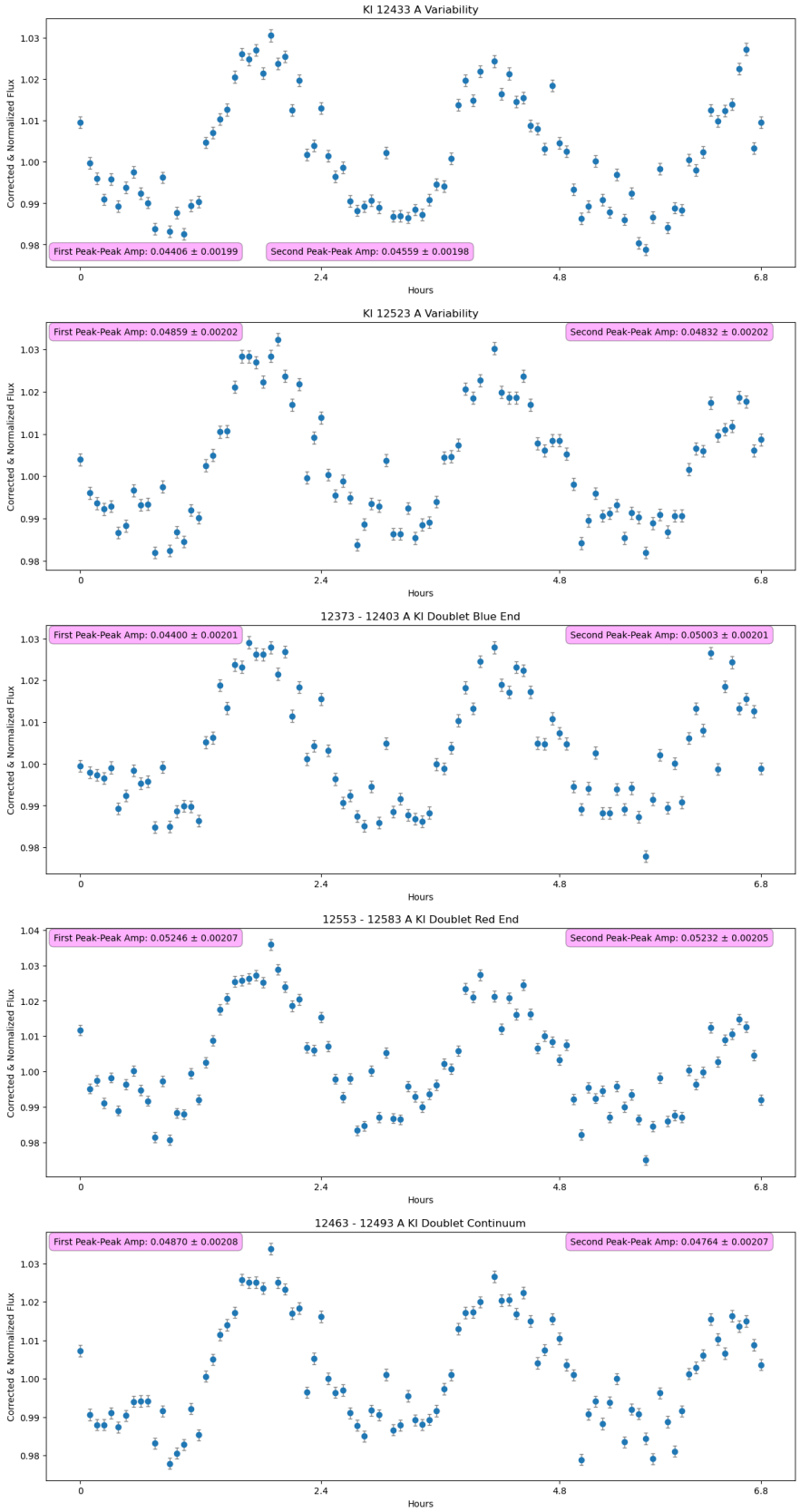

Figure 7: For November: Variability of the potassium doublet absorption lines (first then second), variability of 30 Å on the blue end of the doublet, variability of 30 Å on the red end of the doublet, and variability of the continuum between the first and second absorption lines.

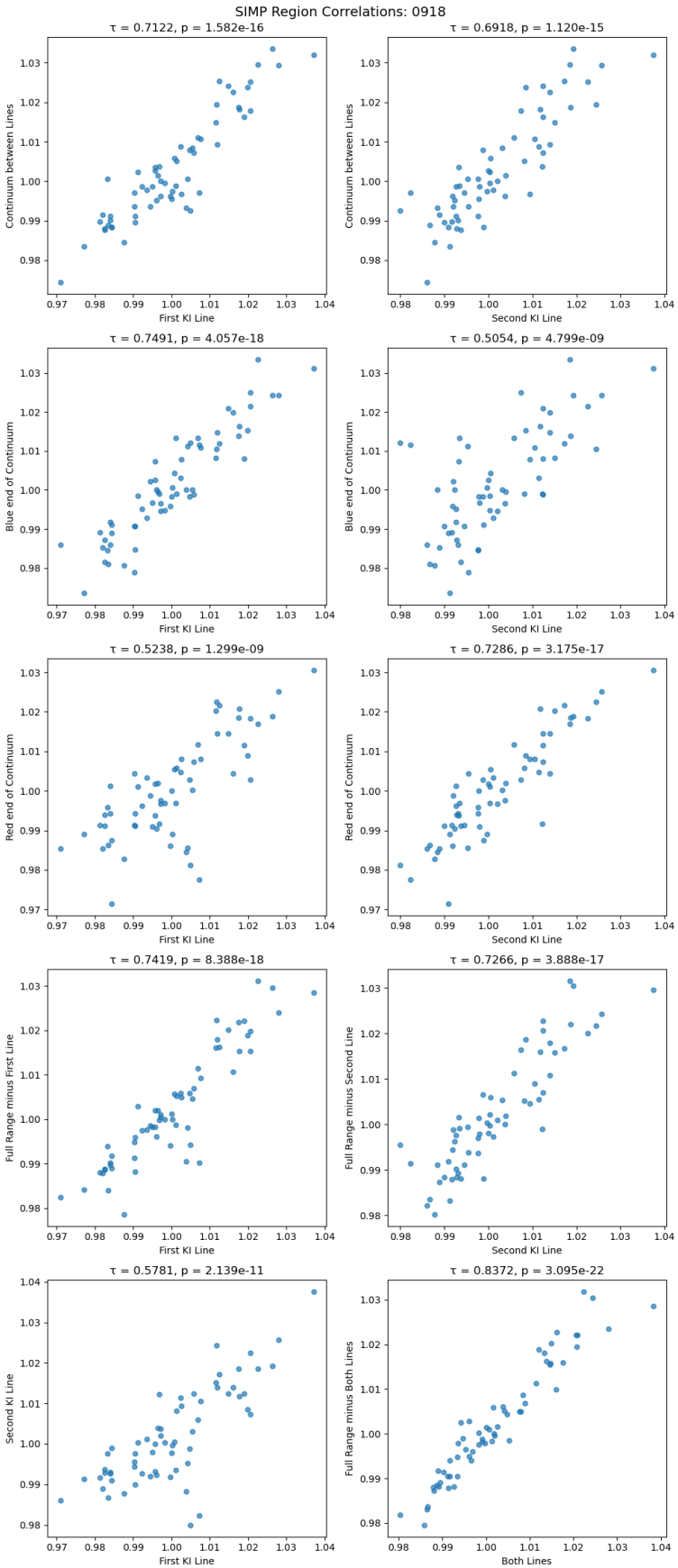
SIMP Region Correlations: 0918
τ = 0.7122, p = 1.582e-16
Continuum between Lines
First KI Line
τ = 0.6918, p = 1.120e-15
Continuum between Lines
Second KI Line
τ = 0.7491, p = 4.057e-18
Blue end of Continuum
First KI Line
τ = 0.5054, p = 4.799e-09
Blue end of Continuum
Second KI Line
τ = 0.5238, p = 1.299e-09
Red end of Continuum
First KI Line
τ = 0.7286, p = 3.175e-17
Red end of Continuum
Second KI Line
τ = 0.7419, p = 8.388e-18
Full Range minus First Line
First KI Line
τ = 0.7266, p = 3.888e-17
Full Range minus Second Line
Second KI Line
τ = 0.5781, p = 2.139e-11
Second KI Line
First KI Line
τ = 0.8372, p = 3.095e-22
Full Range minus Both Lines
Both Lines

Figure 8

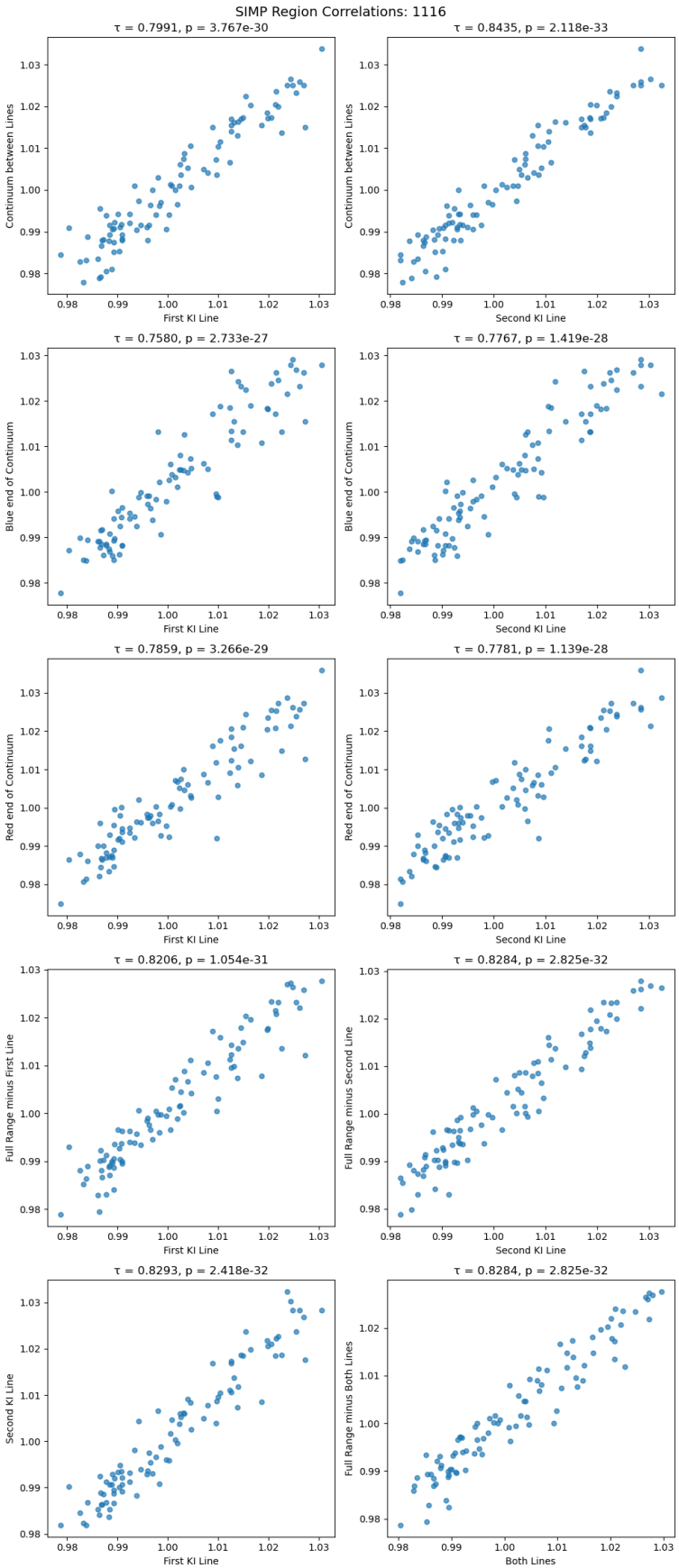
SIMP Region Correlations: 1116
τ = 0.7991, p = 3.767e-30
Continuum between Lines
First KI Line
τ = 0.8435, p = 2.118e-33
Continuum between Lines
Second KI Line
τ = 0.7580, p = 2.733e-27
Blue end of Continuum
First KI Line
τ = 0.7767, p = 1.419e-28
Blue end of Continuum
Second KI Line
τ = 0.7859, p = 3.266e-29
Red end of Continuum
First KI Line
τ = 0.7781, p = 1.139e-28
Red end of Continuum
Second KI Line
τ = 0.8206, p = 1.054e-31
Full Range minus First Line
First KI Line
τ = 0.8284, p = 2.825e-32
Full Range minus Second Line
Second KI Line
τ = 0.8293, p = 2.418e-32
Second KI Line
First KI Line
τ = 0.8284, p = 2.825e-32
Full Range minus Both Lines
Both Lines

Figure 9

REFERENCES

Apai, D., Karalidi, T., Marley, M., et al. 2017, Science, 357, 683

Artigau, É., Bouchard, S., Doyon, R., & Lafrenière, D. 2009, The Astrophysical Journal, 701, 1534

Faherty, J. K., Cruz, K. L., Rice, E. L., & Riedel, A. 2013, Proceedings of the International Astronomical Union, 8, 36

Gagné, J., Faherty, J. K., Burgasser, A. J., et al. 2017, The Astrophysical Journal Letters, 841, L1

Helling, C., & Casewell, S. 2014, The Astronomy and Astrophysics Review, 22, 80

Luhman, K. L. 2012, Annual Review of Astronomy and Astrophysics, 50, 65

Manjavacas, E., Karalidi, T., Vos, J. M., Biller, B. A., & Lew, B. W. 2021, The Astronomical Journal, 162, 179

Metchev, S., Apai, D., Radigan, J., et al. 2013, Astronomische Nachrichten, 334, 40

Prochaska, J. X., Hennawi, J. F., Westfall, K. B., et al. 2020, arXiv preprint arXiv:2005.06505